SURVEY OF POST-IRRADIATION EXAMINATIONS MADE OF MIXED CARBIDE FUELS

M. COQUERELLE
Institute for Transuranium Elements,
European Commission,
Karlsruhe

Abstract

Post-irradiation examinations on mixed carbide, nitride and carbonitride fuels irradiated in fast flux reactors Rapsodie and DFR were carried out during the seventies and early eighties.

In this report, emphasis was put on the fission gas release, cladding carburization and head-end gaseous oxidation process of these fuels, in particular, of mixed carbides.

1. Introduction

During the seventies and early eighties, the European Institute for Transuranium Elements has been involved in the development of potential fuels for LMFBR. These studies covered a large spectrum going from the fabrication to the determination of the thermodynamic and thermophysical properties, irradiation in fast flux reactors and, finally, post-irradiation examinations associated with modelling works.

Advanced liquid-metal fast breeder reactor (LMFBR) fuels of the type (U, Pu)$C_{1-x}N_x$ (carbide, carbonitride, and nitride) have been studied in the DN1 and DN2 irradiation experiments carried out in Rapsodie and Dounreay. This paper presents information on fission gas release and a correlation with the different structural regions of these highly rated MX-type fuels. Complementary information concerning the cladding carburization and the head-end gaseous oxidation as possible reprocessing procedure are shortly discussed.

2. Fission gas release

The DN1 and DN2 experiments investigated and compared the behavior of advanced fuels in a fast flux under conditions of high linear power (X_{max} = 1.3 x 10^2 kW · m^{-1} with a pellet diameter of 8.3 mm). The DN1 experiment was performed in DFR and investigated helium-bonded (U, Pu)N, (U, Pu)C and (U, Pu)$C_{1-x}N_x$ fuels (x = 0.2, 0.5 and 0.8); the maximum burn-ups achieved ranged from 1.3 to 7.8 at. %.

The DN2 experiment was carried out in Rapsodie and investigated helium-bonded (U, Pu)$C_{1-x}N_x$ fuel (x = 0.2 and 0.5); the maximum burn-ups attained ranged from 1 to 4 at. %. Fuel pin specifications are summarized in Table I.

2.1 Experimental

Analysis of Released Gas

The released gas contained in the plenums of all sound pins from the DN1 and DN2 experiments was analyzed. The amount of gas in the plenum was measured volumetrically, and mass spectrometry was used to determine the isotopic composition of the gas. The equipment used for puncturing the cladding and collecting the gas has been described elsewhere [1].

Analysis of Retained Gas

Gas chromatography was used to determine the integral amount of gas present and the concentrations of xenon and krypton. The local concentration of bonded xenon (that dissolved in the fuel

lattice and present in gas bubbles) and its variation with radial position was determined by electronprobe microanalysis (EPMA). The analysis of krypton is not possible because interference exists between the krypton $L\alpha_1$ X-ray line and the uranium 2 $M\alpha_1$ line from the fuel matrix. Furthermore, the krypton $L\alpha_1$ line is difficult to detect above the active background of the specimen.

The analysis of retained gas by chromatography was restricted to six pin sections (five sections of carbonitride and one of nitride fuel; see Table II). Likewise, the analysis of bonded xenon by EPMA was carried out on three sections of sodium-bonded carbonitride fuel (two sections from pin CNP and one from ENP), one section of helium-bonded nitride fuel (from pin AP3), and one section of helium-bonded carbide fuel (from pin DP1).

Gas Chromatography

The fission gas retained in pellet size samples of known weight was liberated in a two-stage operation. First, the fuel was ground to a powder with a grain size < 1 μm, and then the powdered fuel was dissolved in concentrated nitric acid. At each stage, the gases escaping were collected on a cold trap and analyzed for Xenon and krypton. The first stage (grinding) gave information about the amount and composition of the fission gas contained in pores < 1μm in size; the second stage (dissolution) gave similar details for the bonded gas.

TABLE I

Fuel Pin Specifications

Experiment		DN1			DN2	
Fuel	U/(U + Pu) (wt%)	20			20	
	$^{235}U/U$ (wt%)	93			88	
	Form	Pelletized	Vibrocompacted	Covibrated	Pelletized	Covibrated
	Fuel density (%TD)	85-89	---	---	86-89	---
	Smear density (%TD)	81-85	79-80	78	82-85	80-83
	Pellet diameter (mm)	8.3	---	---	8.3 8.0	---
	Fuel stack length (mm)	475			320	
Fuel-to-cladding	Bonding gap (μm)	He 200			Na 500	He 200
Cladding	Material	DIN 1.4919 stainless steel				
	o.d. (mm)	9.5				
	i.d. (mm)	8.5				
Fuel pin	Overall length (mm)	790			726	
	Void volume in plenum (cm^3)	10				

TABLE II

Concentrations of Xenon and Krypton in Retained Gas

1	2	3		4		5	6	7
		Gas in Pores		Bonded Gas				
Pin Section	Fuel Type	Kr	Xe	Kr	Xe	Xe/Kr Bonded Gas	Xe/Kr Gas in Pores	Xe/Kr Gas in the Plenum
		(mm^3/g-fuel)						
CP2/7.2	$MC_{0.5}N_{0.5}$	16.68	104.9	54.23	391.2	7.21	6.28	6.42
ANP/3.2	MN	20.98	126.7	55.56	395.1	7.11	6.03	
ENP/4.2	$MC_{0.8}N_{0.2}$	13.20	77.9	86.32	616.4	7.14	5.90	5.587
CNP/1.7	$MC_{0.5}N_{0.5}$	15.68	94.55	58.31	439.0	7.52	6.02	6.082
CNP/3	$MC_{0.5}N_{0.5}$	13.76	81.41	28.54 (?)	317	11.11	5.91	6.082
CNP/6	$MC_{0.5}N_{0.5}$	7.29	44.59	82.73	590.7	7.14	6.10	6.082

EPMA

The electronprobe microanalyzer at the Institute for Transuranium Elements is a shielded Cameca MS46. Xenon analysis was carried out at electron acceleration potentials > 15 kV and at beam currents of 300 and 500 nA. Since a suitable standard material for xenon analysis by EPMA does not exist, the $L\alpha_1$ X-ray intensity from pure xenon was obtained by interpolation of the $L\alpha_1$ intensities from a series of elements on each side of xenon in the periodic table. To compensate for small day-to-day changes in the operating conditions of the machine, the intensities measured were related to the intensity from pure antimony.

The analysis results were corrected using the ZAF program of Tong. The $L\alpha_1$ absorption coefficients for xenon absorption in uranium and plutonium were interpolated from the values for iodine and cesium $L\alpha_1$ absorption. A detailed description of the analytical method is given elesewhere.

2.2 Xenon Release from Helium-Bonded Pins

At low burn-up (< 1.5 at. %), xenon release is dependent on the chemical composition of the fuel (Fig. 4). Release is greatest from (U, Pu)C (~ 75 %) and least from(U, Pu)N (35 %). The fraction of xenon released from (U, Pu)$C_{1-x}N_x$ fuel is between that from (U, Pu)N and (U, Pu)C fuels (Fig. 4). For these fuels, xenon release increased sharply with carbon content up to x = 0.5. Further increase in carbon content did not significantly change the fraction of xenon released (Fig. 1).

For carbide and carbonitride fuels with x < 0.8, the fraction of xenon released is larger at low burn-up than at medium burn-up. For carbon-rich fuels, x < 0.5, the difference in the fractions of xenon released at low and medium burn-up was ~ 30 % absolute. The lower xenon release at medium burn-up is most probably due to a drop in fuel centerline temperature (~ 400 K) following fuel-cladding contact.

Concentrations of Xenon and Krypton in Retained Gas

The results of gas chromatography are given in Table II. It is evident from the ratios of the xenon and krypton concentrations (cf., columns 5 and 6) that gas in pores contains proportionally more krypton than bonded gas. For the purpose of comparison, column 7 lists the xenon/krypton concentration ratios for the gas contained in the plenums of the pins. As expected, the ratios are very similar to those given in column 6, corroborating the fact that the gas travels to the plenum by way of interconnected pores. Furthermore, a comparison of the gas concentrations listed in columns 3 and 4 of Table II reveals that for carbonitride fuel, < 20 % of the retained gas is held in pores; the bulk of the gas is contained in bubbles or dissolved in the fuel lattice.

2.3 Fuel Restructuring

In the DN1 and DN2 irradiations, the radial temperature difference between the center and the surface of the fuel was in the range from 700 to 1000 K. Furthermore, consideration of the cladding temperature and the fuel-cladding heat transfer coefficient, h, indicates that the fuel surface temperature lay between 1000 and 1300 K. This gives a range for the in-pile fuel temperature of 1000 to 2300 K.

Figures 2 and 3 show examples of the structural zones in the carbide pin DP1 and the nitride pin AP1 after 6.5 and 5 at. % burn-ups, respectively. The kinetics of fuel restructuring are faster in carbon-rich fuels because the coefficients of self-diffusion for uranium, plutonium and carbon are larger than in nitrogen-rich fuels.

Ceramographic analysis of the 21 pins irradiated revealed the presence of four distinct structural zones, each of which is associated with well-defined restructuring processes. These zones, which have been designated I through IV, are characterized by the following structural features.

Zone IV. Stable grain size and relatively stable fabrication porosity. Densification, if present is associated with a decrease in the number of pores with a size smaller than 2 μm. The upper temperature limit for this zone, T_{IV}, is a function of burn-up and of the chemical

composition of the fuel. In the case of (U, Pu)C fuels, T_{IV} is ~ 1000 K for a fuel irradiated to a burn-up of 6 at. % and ~ 1300 K for a fuel irradiated to a burn-up of 1 at. %. In MN fuels, TIV is ~ 250 K higher than in MC fuels irradiated under similar conditions.

Table 3. Details of the oxidations and final reaction products

Fuel composition	average burn-up (a/o)	Oxidation conditions: Atmosphere	average temp. (°C)	Total time (h)	Complete oxidation	O/M from X-ray diffraction	Structure of final products
(U,Pu)N	1.41	CO/CO_2	800	8	✓		
"	1.41	"	816	13	✓		
"	4.46	"	750	8	Na in Pin		
"	1.20		800	19	**	2,01±0,01	(single
$(U,Pu)C_{0.8}N_{0.2}$	1.04	"	800	11	✓	2,01±0,01	(phase
"	2,83	"	800	12	**	2,01±0,01	(fluorite
$(U,Pu)C_{0.9}N_{0.1}$	1,02	"	750	8	✓		(structure
"	1.81	"	880	18	✓		
(U,Pu)C	1.41	"	750	8	✓	2,00±0,01	
(U,Pu)N	4,46	Ar-20%O_2	590	13	Na in Pin		single phase fluorite
"	3,45	"	"	23	✓		
$(U,Pu)C_{0.8}N_{0.2}$	1.04	"	"	16	✓		)two phase
"	2.83	"	"	16	**		)MO_{2+x}(50%)
$(U,Pu)C_{0.9}N_{0.1}$	1,02	"	"	20	✓		)and M_3O_8
"	1,81	"	"	12	✓		) 50%)

* Samples were weighed at intervals during the oxidation. Oxidation was considered to be complete when there was no further change in weight of the sample. Particles were removed from the reaction vessel during weighing intervals for examination by optical microscopy.

** Small quantity of material lost from reaction vessel.

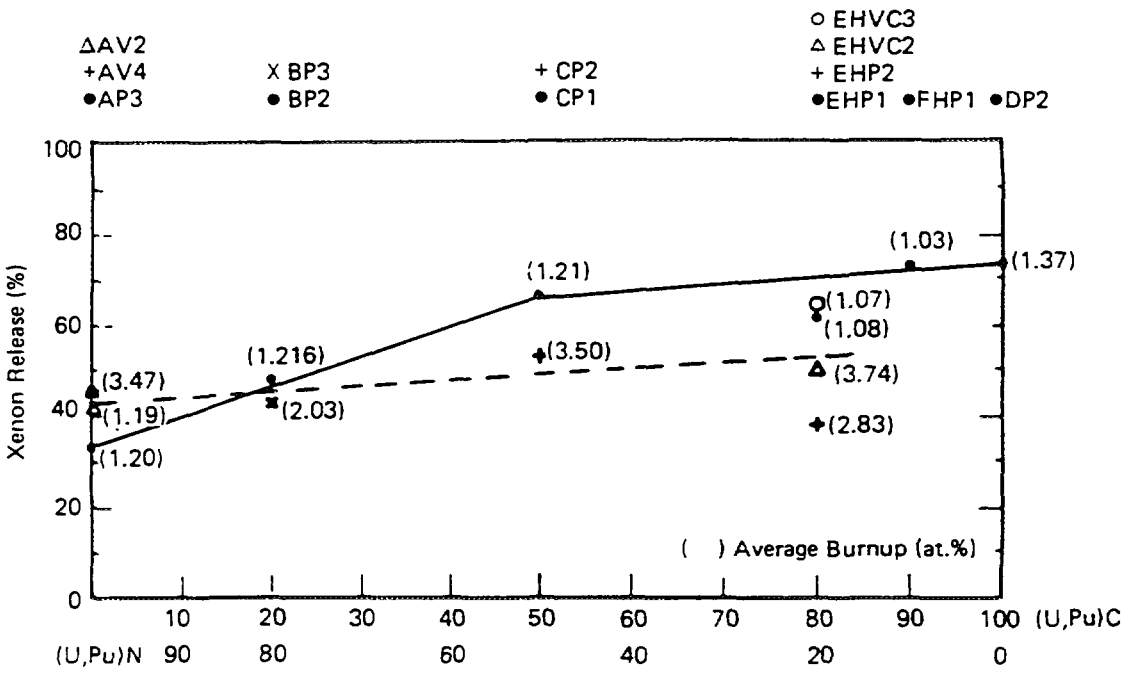

Fig. 1. Xenon release related to fuel composition and burnup.

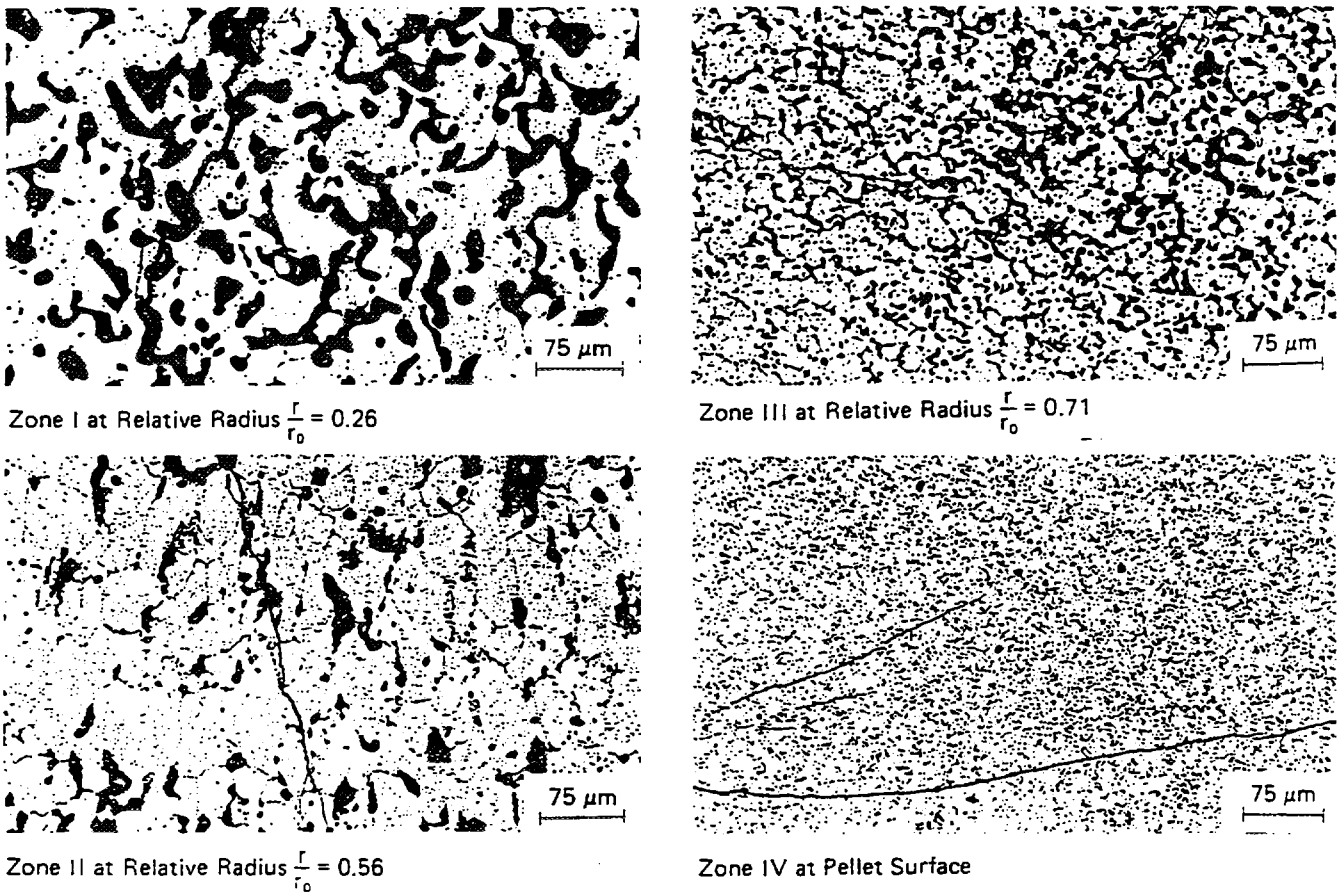

Fig. 2. Restructuring as a function of radial position in a mixed carbide fuel. Local linear power 90 $kW \cdot m^{-1}$. Local burnup 6.5 at.%.

Zone III. Restructuring occurs mainly by coaxial grain growth. This is associated with an increase in porosity, which takes place in the following stages, given in the order of increasing radial temperature:

1. increase in the population of pores with diameters < 1 μm and > 5 μm
2. pore precipitation at grain boundaries as a consequence of enhanced gas mobility
3. coalescence of pores at grain boundaries perpendicular to the thermal gradient leading to broadening of such boundaries and to break-away swelling.

Zone II. Preferential grain growth occurs parallel to the radial temperature gradient, and radial alignment of fission gas porosity takes place at grain boundaries. This zone resembles the columnar grain structure generally found in mixed-oxide fuels, and is particularly well developed in carbon-rich fuels where evidence for pore migration has been observed (see Fig. 4).

Zone I. Region of coarse fission gas porosity and high gas release. Large asymmetric (globular) pores form that are similar in size to the fuel grains ($\leq$20 μm). As in zone II, grains may possess a fine 'porosity' (< 1 μm in diameter) due to fission gas precipitation in a heterogeneous distribution.

The zones are described in the order in which they appear in the fuel with increasing distance from the surface (i. e., in the order of increasing radial temperature).

Finally, it is pointed out that a small central hole formed in the nitride fuels and in nitrogen-rich carbonitride fuels with x > 0.8. In contrast to oxide fuels, where the central hole results from the migration of lenticular pores up the radial temperature gradient, the central hole in nitride fuels is apparently created by a sintering mechanism.

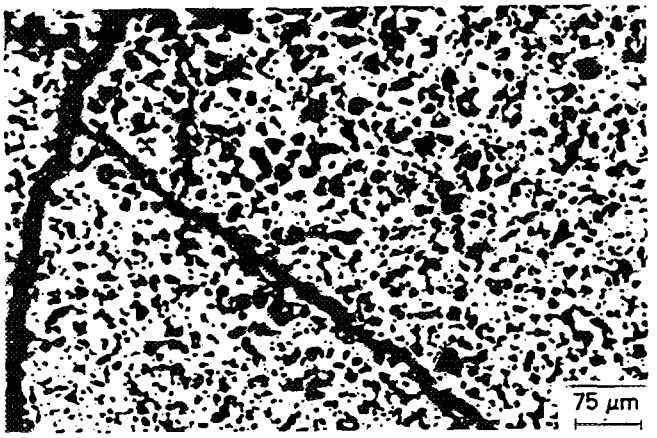

Zone I at Relative Radius $\frac{r}{r_0} = 0.10$

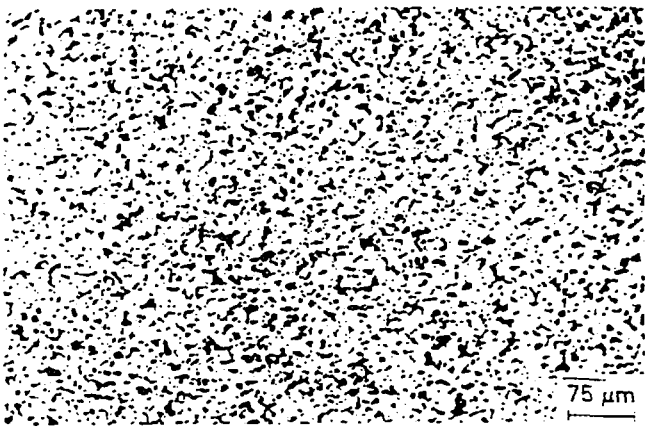

Zone III at Relative Radius $\frac{r}{r_0} = 0.54$

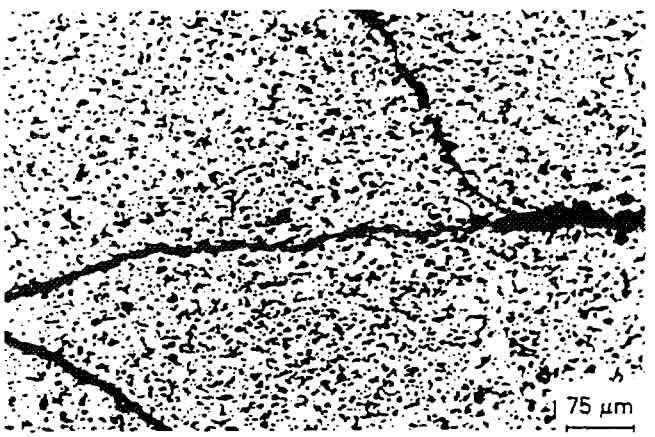

Zone IV at Pellet Surface

Fig. 3. Restructuring as a function of radial position in a mixed nitride fuel. Local linear power 120 $kW \cdot m^{-1}$. Local burnup 5.0 at.%.

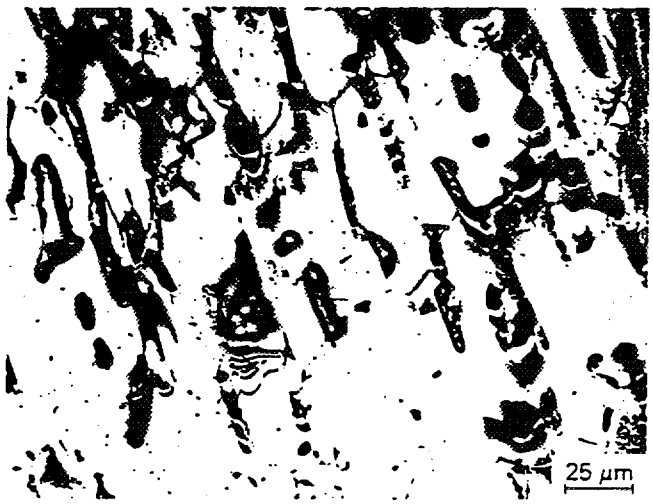

Fig. 4. Pore migration in a mixed carbide fuel. Local linear power 130 $kW \cdot m^{-1}$. Local burnup 1.5 at.%.

2.4 Radial Distribution of Retained Xenon: Correlation with Fuel Structure

(U, Pu)C_{1+x} (Helium-Bonded)

The general form of the distribution profile shown in Fig. 5 is similar to that of xenon profiles obtained from sodium-bonded carbonitride fuels (Fig. 6). The fuel exhibited the four structural zones first defined by Ronchi and Sari (Ref. 2); their radial positions are also marked in Fig. 5. The dense outer fuel (zone IV) consisted of regions with high and low concentrations of xenon. Accordingly, on the left side of the profile, the concentration of xenon approaches the nominal fast fission yield of 0.62 wt % (value after a cooling period of 3 yr.); on the right side, over a distance of 650 μm , the xenon concentration falls sharply from 0.57 to 0.26 % at the fuel surface. In the central porous fuel region (zones I and II), the concentration of xenon was ~ 20 % of the amount created by fission. As in the case of the nitride and carbonitride fuels, the transition from xenon concentrations close to the fission yield to the low concentrations found in the central porous fuel occurred in zone III. The integrated xenon release for the pin section was 50 %, which is slightly lower than the gas release value extrapolation from Fig. 1.

The reason for regions of low xenon concentration at the fuel surface is not well understood. Such regions, however, had a lower density than fuel regions with xenon concentrations approaching the nominal fission yield. This suggests that the observed decrease in retained xenon concentration could, in part, be due to a fall in the amount of xenon created.

The decrease in fuel density was associated with the formation of two actinide containing phases. One phase was confined to a region within 100 μm of the fuel surface and was apparently an oxide; the other phase was probably sesquicarbide.

It is worth noting that the forms of the cesium and xenon profiles measured along the same diameter were almost identical. This indicates that the cesium, which results mainly from the decay of ^{133}Xe and ^{135}Xe, is trapped in small gas bubbles and pores. More significantly, the finding suggests that in advanced fuel the behavior of cesium closely resembles that of xenon.

(U, Pu)($C_{0.5}N_{0.5}$) (Sodium-Bonded)

The radial distribution profile contained in Fig. 6 exhibits two distinct concentration regions:

1. a region in the porous fuel zone between $r/r_0 = 0.6$ and the fuel center, in which the xenon concentration is ~ 40 % of the created amount

2. a region in which the amount of bonded xenon is close to the calculated fast fission yield of 0.42 wt % (value after a cooling time of 3 yr.).

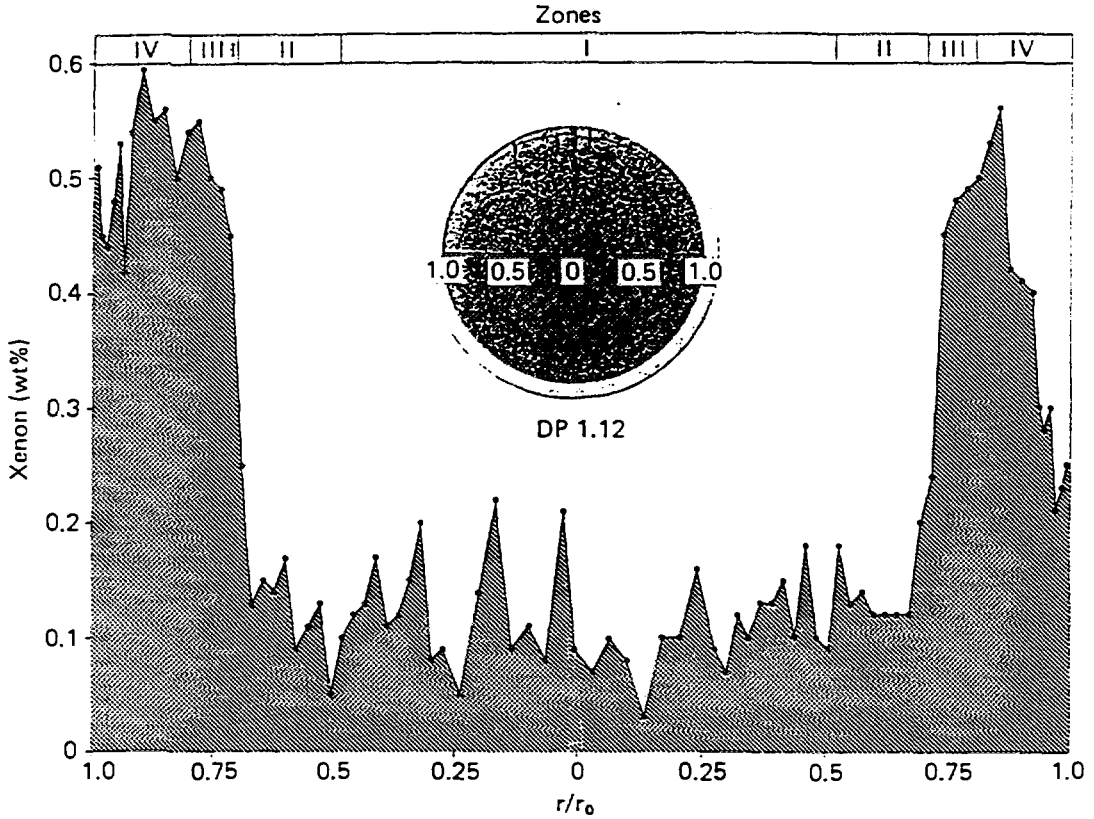

Fig. 5. Radial distribution of xenon in a helium-bonded fuel of composition $(U_{0.8}Pu_{0.2})C_{1+x}$. Local linear power 105 $kW \cdot m^{-1}$. Local burnup 5.8 at.%.

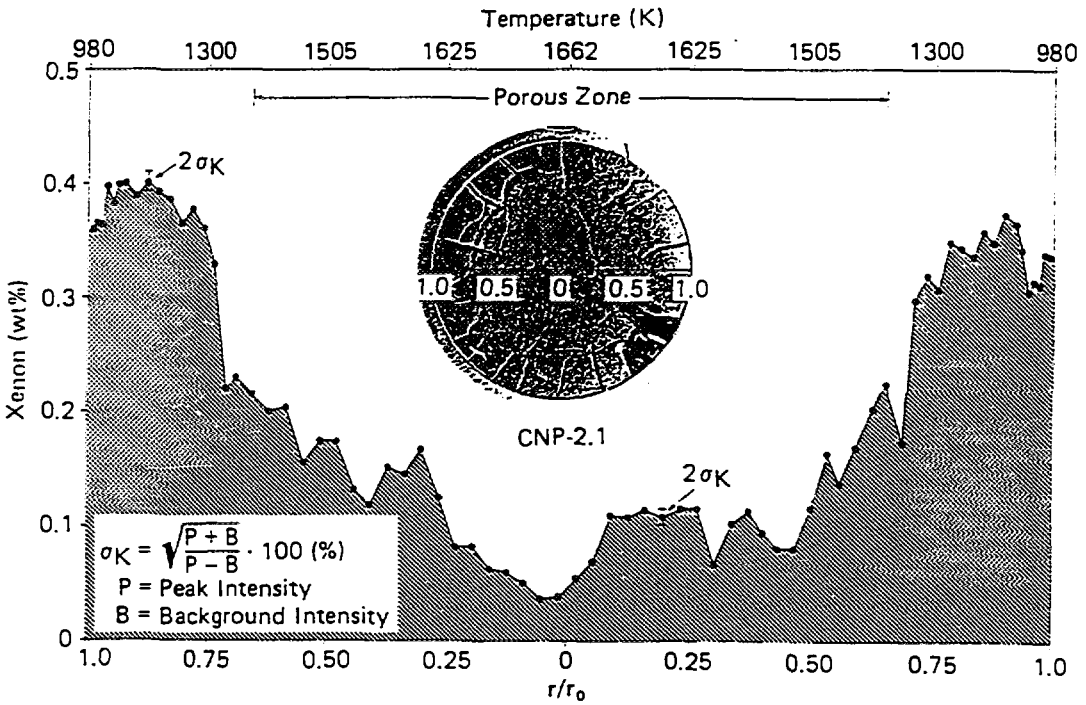

Fig. 6. Radial distribution of xenon in a sodium-bonded fuel of composition $(U_{0.8}Pu_{0.2})(C_{0.5}N_{0.5})$. Local linear power 125 $kW \cdot m^{-1}$. Local burnup 3.8 at.%.

This region extends almost from the fuel surface to $r/r_0 = 0.75$ in the outer dense fuel zone; within 50 μm of the fuel surface, a small decrease in xenon concentration occurs.

The region $0.6 < r/r_0 < 0.75$ is a transitional zone in which the xenon content of the fuel falls sharply from concentrations approaching the fission yield to the low concentrations found in the central porous regions. The range of this zone is not well defined, although the main concentration step occurs in structural zone III. The integrated xenon release for the pin section was 36 %.

(U, Pu)N (Helium-Bonded)

The radial distribution profile shown in Fig. 7 indicates that release behavior in a nitride fuel is similar to that outlined for carbide and carbonitride fuels. In contrast to the last two fuels, however, the nitride fuel contained a small central hole and exhibited only two of the four structural zones, namely, zone III (intergranular porosity) and zone IV (unrestructured fuel). The bulk of the fuel consisted of structural zone III. This extended from the central hole to $r/r_0 = 0.85$. In this region xenon release was on the order of 45 %, whereas in the remaining structural zone IV, which occupied the outer part of the fuel, only ~ 15 % of xenon created was released. The integrated xenon release for the pin section was 30 to 35 %. This is in good agreement with the gas release value obtained by chromatography (see Fig. 1).

Some Comments on the Mechanisms of Gas Release

Most irradiation experiments undertaken to investigate mixed carbide and nitride fuels have been carried out at a power below 90 kW · m^{-1}, which produced a fuel centerline temperature lower than 1400 K. The pins dealt with in this paper were mainly helium-bonded and were irradiated at high linear power (135 kW · m^{-1} maximum). This led to high central temperatures of 2300 K at the start of irradiation and 1900 K after gap closure. Thus, the DN irradiations can be considered to have consisted of two stages that were characterized by pin operation under distinct different temperature conditions. In the first stage of irradiation, when the gap was open (h = 0.5 to 1.0 x10^{-4} W · m^{-2} · K^{-1}), fuel restructuring occurred and the formation of interconnected porosity took place at fuel temperatures above 1100 K. From the standpoint of fission gas release studies, the latter constitutes the structural feature of principal interest.

The second stage of the irradiation, which we consider to be the steady-state temperature condition, was associated with the closure of the gap and an increase in value of the thermal transfer coefficient, h, to 2 x 10^{-4} W · m^{-2} · K^{-1}. The subsequent drop in fuel temperature of ~ 400 K modified the rate of all thermally activated mechanisms. It is to be noted, however, that the structural features developed in the first stage of the irradiation were retained in this second stage.

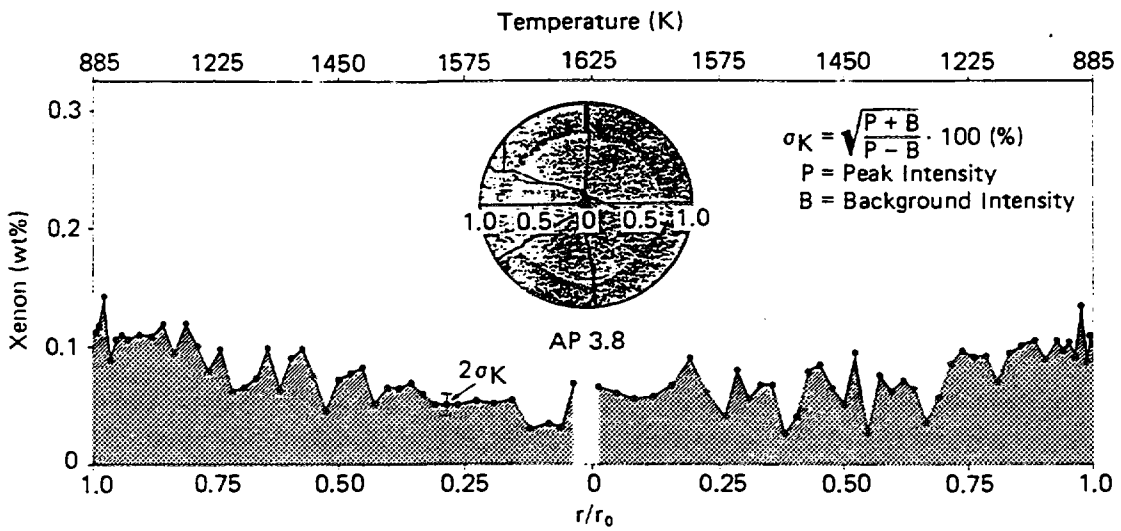

Fig. 7. Radial distribution of xenon in a helium-bonded fuel of composition $(U_{0.8}Pu_{0.2})N$. Local linear power 115 kW·m^{-1}. Local burnup 1.1 at.%.

The mechanisms that can be postulated for fission gas release are of two different kinds:

1. mechanisms such as atomic diffusion and pore migration (by diffusion or evaporation-condensation) that are thermally activated

2. mechanisms such as transport by recoil and knock-on that are related to the fission process; these can play a role in the central region of the fuel where the free surface offered by the interconnected porosity becomes important.

From the post-irradiation examination of the DN pins, evidence has been obtained for gas transport by atomic diffusion. Gas chromatography of bonded xenon has revealed that the gas in pores contains proportionally more krypton than bonded gas (Table II). This finding can be explained if it is recognized that in fuel the diffusion rate of krypton is faster than that of the larger atom, xenon. It is unlikely that bubble migration, if it occurs, can produce such a shift in the composition of the retained gas.

Fission gas bubbles in carbide and nitride fuels grow rapidly to size at which their mobility becomes extremely low. Both theory and experimental observation indicate that in technologically significant periods of time the motion of bubbles > 100 Å in size is confined to negligible root-mean-square distances. In fact, during irradiation the walls of large bubbles become contaminated by precipitated or segregated fission products, and, consequently, the truly effective mechanism of bubble migration is volume diffusion, which produces slow migration rates [e. g., between 10^{-12} and 10^{-13} ms^{-1} at 2300 K in (U, Pu)C with $\Delta T = 1300\ K \cdot cm^{-1}$ (Ref. 3)].

A second mechanism, bubble sweeping, is provided by the direct motion pores that, by evaporation-condensation, migrate at higher rates than small bubbles. The sweeping of bubbles has the effect of transferring gas and void volume to grain boundaries or to interconnected porosity. Post-irradiation work indicates that this mechanism occurs in carbide fuel and carbonitride fuels with low nitrogen contents ($x < 0.2$). It operates in a limited temperature range corresponding to structural zone II (Ref. 7), where bubbles grow rapidly to a large size, but does not play a determining role in the total gas release because sweeping does not occur at a sufficiently high rate. Thus, it can be concluded that bubble migration makes only a small contribution to fission gas release.

A more detailed discussion on the mechanism aspects can be found in Ref. 4.

2.5 Conclusions

The investigation of fission gas release from carbide, carbonitride, and nitride fuels irradiated in a fast flux under conditions of high linear power has enabled the following conclusions to be drawn:

1. At low burn-up, xenon release from helium-bonded advanced fuel is dependent on the chemical composition of the fuel.

2. At medium burn-up, closer fuel-cladding contact in helium-bonded pins leads to a decrease in the fraction of gas released from (U, Pu)$C_{1-x}N_x$ fuel with $x < 0.8$.

3. In advanced fuels, more than 75 % of the retained fission gas is contained in gas bubbles and in the fuel lattice. The remaining gas that is trapped in pores contains proportionally more krypton than the bonded gas. Gas is mainly released to the plenum by way of interconnected pores.

4. The most important parameter determining fission gas release is fuel structure. The fraction of xenon released from the outer unrestructured region of the fuel is generally lower than 15 %; the mechanism controlling the release appears to be atomic diffusion. The fraction of xenon released from the central porous region is 50 % and more, and is highly dependent on the composition of the fuel and on burn-up. In this region, the role of interconnected porosity is determining. Besides diffusion, such supplementary mechanisms as bubble sweeping by grain

boundary or pore migration as well as recoil and knock-on due to fission promote the transfer of xenon and krypton to the interconnected porosity.

References

1. M. Coquerelle, 'The Alpha-Beta-Gamma Laboratory of the European Institute for Transuranium Elements: Equipment Used for the Post-Irradiation Examination of Plutonium Fuels', *Proc. 15th Conf. Remote Systems Technol.*, 246 (1967)

2. C. Ronchi and C. Sari, 'Swelling Analysis of Highly Rated MX-Type LMFBR Fuels. 1. Restructuring and Porosity Behaviour', J. Nucl. Mater., **58**, 140 (1975)

3. C. Ronchi, I. L. F. Ray, H. Thiele, and J. van de Laar, 'Swelling Analysis of Highly-Rated MX-Type LMFBR Fuels', J. Nucl. Mater., **74**, 193 (1978)

4. M. Coquerelle and C. T. Walker, 'Fission Gas Release and Microscopic Swelling in highly rated Advanced Fuels', **48**

3. Cladding carburization

3.1 Experimental analyses of irradiated stainless steel cladding of sodium-bonded pins

The cladding material used in the irradiation experiments examined were two solution annealed Type 316 (17 Cr, 14 Ni) type steels. Stabilized steels (DIN 1.4790, DIN 1.4988) were also tested or analyzed occasionally. The irradiations were carried out in the Rapsodie and Dounreay fast reactors.

Chemical analyses of the total carbon content, electron microprobe analysis, and microhardness measurements were carried out on the cladding steel of pins irradiated at burn-ups ranging from 2.6 to 12.5 % fima and linear powers between 80 and 100 kW/m.

The following results were obtained:

1. In the range up to 120.000 Mwd/ton, the total carbon content of the cladding increases linearly from 300 to 5000 ppm. The carburization stops at high burn-up, when all the excess carbon (4 % M_2C_3 was typically present in the starting fuel) is transferred to the cladding.

2. After an irradiation time of ~ 200 days, the carbon concentration at the cladding surface attains a value of 1.5 % and thereafter does not change appreciably (Fig.8).

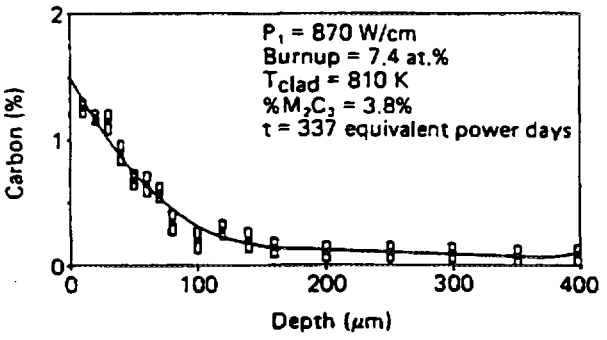

Fig. 8 Typical carbon penetration profile in a stainless steel cladding (from microprobe measurements) of a sodium-bonded pin at high burnup. At first glance this type of profile might be analyzed in terms of a simple linear diffusion process.

3. The shape of the carbon concentration profile as a function of the penetration depth is similar to that obtained in diffusion measurements with constant surface concentration (Fig. 8). This suggests that the carbon is supplied by the fuel at a sufficiently high rate.

4. Microhardness changes produced by carburization were found at various cladding temperatures. Figure 9 shows the average of 12 measurements taken along a circumference at 30 μm from the inner cladding surface, plotted as a function of the cladding inner temperature. The curves display a maximum in the range between 720 to 750 K. In the case of pins irradiated in Rapsodie, where the inner cladding temperature was always > 770 K, the maximum could not be observed.

3.2 Carbon Reactions in Stainless Steel

The major driving force for the reaction between carbon and stainless steel is provided by the very low free energy of formation of various carbides among which those of the type $(FeCr)_{23}C_6$ are found to play the major role in the carburization processes. Figure 10 shows that the equilibrium carbon activity of $Cr_{23}C_6$ is lower than the carbon activity of a hyperstoichiometric uranium carbide by several orders of magnitude.

In the same figure are plotted the carbon activities of some of the more important carbides formed by the fission products.

The dissociation reaction $M_2C_3 \rightarrow 2\ MC + C$ can therefore be thought to control steel carburization. The penetration and reaction of carbon with the steel components take place through a complex pathway, which, in the temperature range of interest, depends to a large extent on two separate reaction kinetics:

1. diffusion of carbon in the austenitic phase

2. formation of $(FeCr)_{23}C_6$ precipitates within the grains and at grain boundaries.

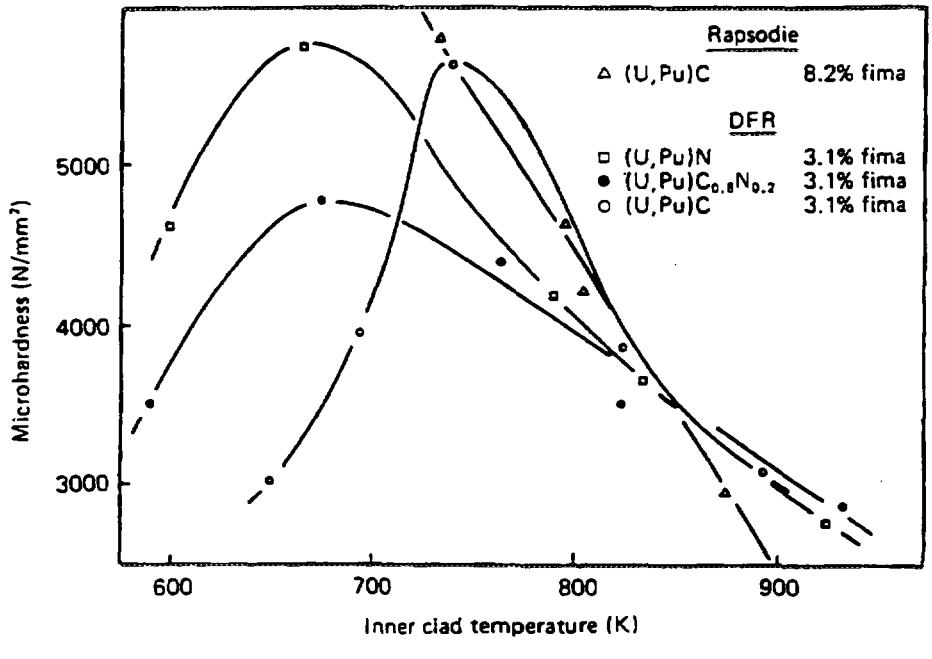

Fig. 9 Average microhardness measured in Type 316 stainless steel claddings, carburized at different temperatures. A maximum hardening is found in a rather well-defined temperature range. See also the section on the interpretation of profiles.

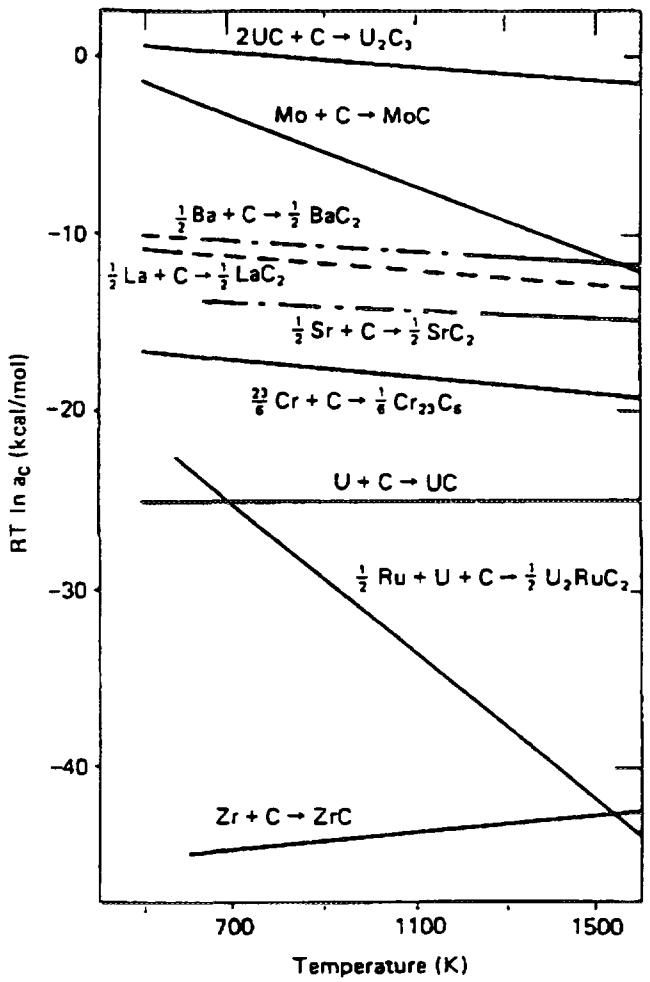

Fig.10 Equilibrium carbon activity as a function of temperature for the most relevant carbon reactions involving fuel components and principal fission products.

The definition and measurement of an effective carbon diffusion coefficient D_{eff} are therefore rather problematic. The shape and the depth of the carbon profile beneath the carburization surface are functions of the space and size distribution of the $(FeCr)_{23}C_6$ precipitates. Therefore, the effective diffusion coefficients obtained from the measured carbon profiles by means of linear diffusion models display a large scatter. Furthermore, the temperature dependence of the diffusion coefficients obtained is very weak; in an Arrhenius plot an activation enthalpy of < 10 kcal/mol is obtained (Fig. 11) that can be hardly attributed to a realistic single activated atomic jump. The analysis of the carbon diffusion equation in the steel from a measured profile should therefore be performed with an adequate algorithm which has been developed by C. Ronchi (Ref. 1).

3.3 Interpretation of the Axial Hardening Profiles of the Cladding

The carburization produces different modifications of the steel mechanical properties, depending on the extent to which the process takes place and on the morphology of the carbides formed.

As shown, the carbon penetration profiles do not change very much in the temperature range 570 to 920 K, in which the cladding normally operates. On the other hand, the microhardness variations as a function of temperature, reported earlier in this paper in observations of sodium-bonded pins, are considerable. They should therefore be attributed to the microstructural changes produced by carburization rather than to the gross amount of carbon diffused into the steel. Starting from Fig.10, three different carburization conditions are expected: These correspond to distinct carburization regimes.

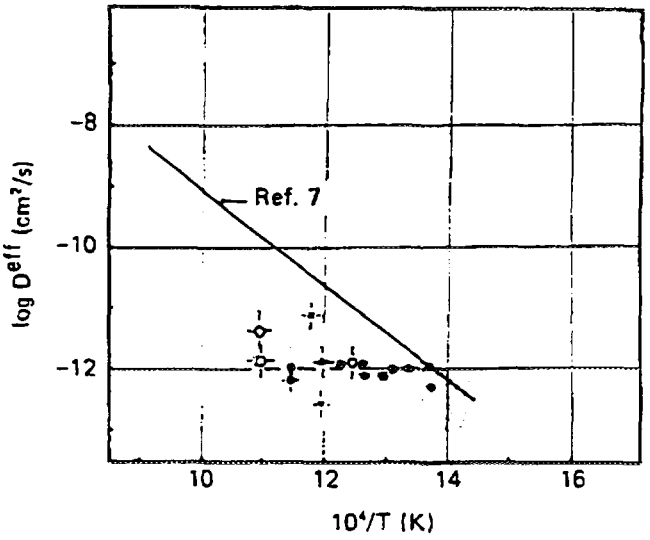

Fig. 11 Arrhenius plot of effective carbon diffusion coefficient in stainless steel obtained from out-of-pile measurements. The data points in the shaded area were deduced from carbon profiles in carburized claddings after irradiation. A different diffusion mechanism is indicated. The line at the top represents the out-of-pile measurements made by Agarwala et al. (Ref. 40).

Low-Temperature Regime (Up to ~ 700 K, see Fig. 9)

This is characterized by an increase of hardness with temperature. At temperatures 550 K the rate of diffusion of carbon is very low ($D_c < 10^{-13}$ cm^2/s), and negligible carbon penetration is expected during typical irradiation times. Only at temperatures > 600 K is the penetration deep enough for carburization to become important.

The optically detected morphological variations of the steel structure produced by carburization are not obvious. In this temperature range the largest microhardness increases are measured, and the carbon penetrating the steel produces a large number of very small intragranular carbide precipitates that are responsible for the observed hardening. The study of precipitation hardening in this temperature range indicates that the amount of carbon precipitated increases strongly with temperature, although the presence or radiation damage was shown to reduce the influence of temperature in the precipitation processes.

Medium-Temperature Regime (700 to 820 K)

The intragranular precipitation of $M_{23}C_6$ attains the maximum extent. At these temperatures the rate of migration of chromium is sufficiently high to produce additional precipitation on the grain boundaries and twins, which increases with temperature. The amount of carbide precipitated on the grain boundaries has little effect on the steel microhardness, which therefore decreases with temperature during this stage in proportion to the fraction of carbon precipitated on the grain boundaries (Fig. 9).

High-Temperature Regime (Above 820 K)

In spite of ist high mobility, the concentration of free carbon and of the submicroscopic carbide particles remains low so that no substantial variations in microhardness with respect to the initial value of 1900 N/mm^2 are expected. On the other hand, the grain boundary reaction with chromium produces a drop of the dissolved carbon concentration in increasingly large zones.

The microhardness curve obtained can be correlated with the frequency of incipient cracks observed in the cladding after diametral deformations of ~ 1 %. Figure 12 shows the frequency of the radial cracks observed in the carburized cladding zone as a function of their depth at different irradiation temperatures. The diagram shows that the largest number of cracks is observed in the temperature zone corresponding to the medium carburization regime, where important hardening is associated with large grain boundary carburization. Actually, the tensile properties of the steel in these conditions are extremely poor. Experiment shows that for carbon concentrations > 0.5 % at temperatures of ~ 750 K the embrittlement is severe and the steel shows very little ductility (Fig. 13) (Refs. 2 and 3).

3.4 Possible Advantages of Cold-Worked Steels

The deterioration of the mechanical properties of the steel caused by carburization is expressed in terms of loss of ductility. If the cladding is expected to be subjected to moderate plastic deformation, however, the major pin failure risks do not arise from precipitation hardening alone but also from severe embrittlement of the grain boundaries. In fact, our observations indicate that the cracks originating at the internal cladding surface have a transgranular character in the heavily carburized zone, but then extend deeper into the steel intergranularly, along carburized grain boundaries. The analysis of the carbon diffusion performed earlier in 'Carbon Reactions in Stainless Steel' suggests that the initial steel defect structure (grain size, twin, and dislocation density) should influence the shape of the carbon penetration profile. Thus, in cold-worked steels a compact intragranular distribution of $(FeCr)_{23}C_6$ precipitates should nucleate and grow on the lattice defects. Finally, a highly carburized layer should be formed down to a certain depth where all the carbon diffusing from the fuel is captured and prevented from penetrating more deeply into the steel.

The effect of cold working on carbon precipitation in sensitizing heat treatments was clearly observed. The carbide precipitation rate is increased by a factor ~ 15 with respect to annealed structures. However, in the presence of radiation damage, the defect structure of the steel is subjected to stubstantial modifications that are not entirely interpreted and quantitatively defined. Generally, the dislocation density of cold-worked steel is observed to decrease with the neutron fluence from typical initial values of 10^{12} to 10^{13} cm^{-2} down to an asymptotical value ρ^* (Refs. 4 and 5).

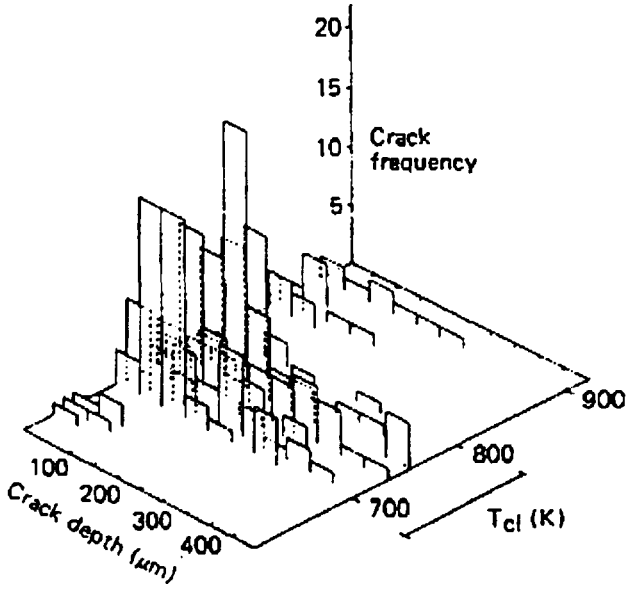

Fig. 12 Frequency of incipient cracks, observed in carburized Type 316 stainless steel claddings, classified according to crack depth and cladding temperature. The cracks were counted in the corresponding sections of 32 mainly helium-bonded pins with burnup ranging between 1 and 8% fima.

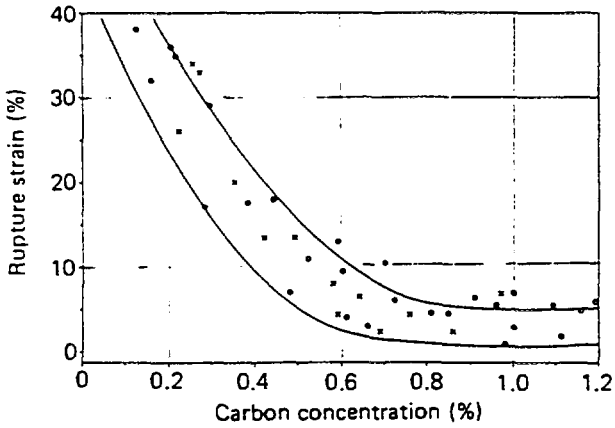

Fig. 13 Decrease of rupture strain with increasing carbon content in Type 316 stainless steel at temperatures between 770 and 1070 K (Ref. 47).

On the other hand, in annealed structures the irradiation produces a progressive increase in dislocation density up to the same value ρ^* ; ρ^* corresponds to the steady-state configurations where an equilibrium is established between creation and precipitation of point defects. The value of is a function of temperature, however, this dependence has not yet been clearly determined.

In some experiments at 770 K and 15 dpa, the dislocation density in cold-worked and solution-annealed Type 316 stainless steel achieves the same order of magnitude of 2 to 5 x $10^{10}/cm^2$. In other experiments on niobium-stabilized steels at 870 K and 16 dpa, the cold-worked dislocation structure was still observed ($\rho \sim 1$ to 4 10^{11} cm^2).

At low temperatures the radiation annealing of the cold-worked dislocations occurs, under standard flux conditions, in relatively long times (more than a few weeks). Above a certain temperature the radiation annealing process is rather rapid with respect to the steel carburization rate; hence the effect of cold-working on carburization is expected to be negligible. This temperature should lie in the range of 850 to 900 K above which extended radiation-induced recrystallization is observed.

It is thus conceivable that up to these temperatures the carbide formation in irradiated steels is accelerated by cold working to form a dense carbide layer preventing a futher deep penetration of carbon, but at higher temperatures the extent of this effect remains unclear.

At the present time, this argument cannot be fully justified. The results obtained in the Los Alamos National Laboratory-Westinghouse tests of fuels fabricated with improved methods seem to confirm that cold-worked steel presents a good carburization resistance. In these experiments a burn-up of 16 % fima was safely attained. Between 670 and 870 K a carburized layer is observed to be formed, independently of temperature, in the early irradiation period, down to a depth of ~100 μm, (20 % of the cladding volume); afterward the carbon penetration does effectively stop. At high burn-up the carburized layer was extensively cracked, but apparently the loss of ductility of the canning was tolerable as diametral strains up to 3.5 % were measured.

On the other hand, British irradiation tests with hyperstoichiometric carbide fuels at burn-ups up to ~ 9 % fima showed that the carburization depths in a 20 % cold-worked Type 316 stainless steel do not exceed 100 μm up to 850 K, but above this temperature they increase abruptly. Similar observations were made on 15 % cold-worked stabilized steels at burn-ups between 5 and 8 % (see the next section) where from 850 to 950 K the carbon penetration depth increases from 100 to 300 μm.

A comparison of the carbon penetration depths in solution-annealed and cold-worked steels is illustrated in Fig. 14. Most of the values of the carbon penetration depths were deduced from microhardness profiles, since at temperatures < 850 K these proved to be strictly homologous to the carbon concentration profiles. The measurements indicate that at low temperatures the solution-annealed steel was subjected to a somewhat deeper carburization than the cold-worked steel, but at > 900 K this difference vanishes.

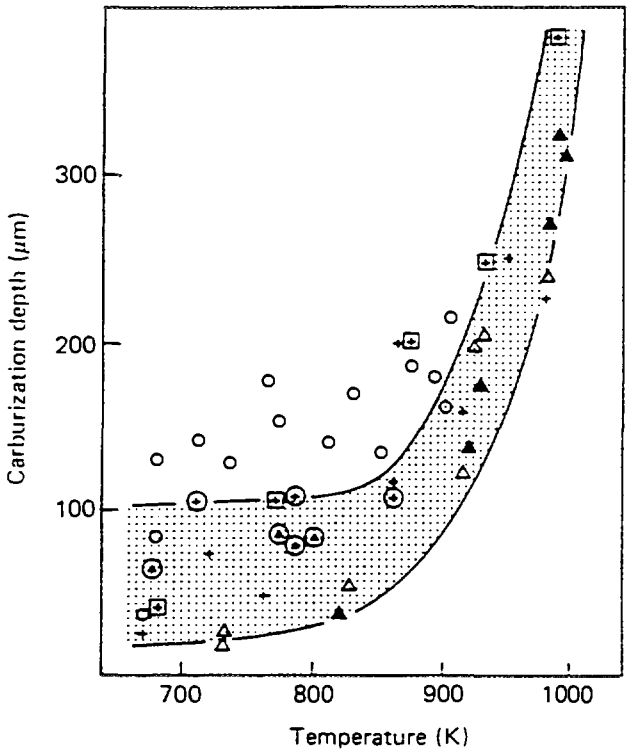

Fig.14 Carburization depth in various cladding steels at medium and high burnup. The data pertaining to cold-worked alloys are in the shaded area:

- ○ = solution annealed Type 316 stainless steel 8 to 12% burnup
- + = cold-worked Type 316 stainless steel 3 to 5% burnup (Refs. 58 and 59)
- ⊞ = cold-worked Type 316 stainless steel 8% burnup (Refs. 58 and 59
- ⊕ = cold-worked Type 316 stainless steel 10 to 12% burnup (Ref. 53)
- △ = cold-worked titanium stabilized 5% burnup
- ▲ = cold-worked niobium stabilized 5% burnup
- ◉ = cold-worked niobium stabilized 7.5 to 9% burnup

3.5 Behavior of Stabilized Steels

Stabilized austenitic steels are being successfully utilized as cladding materials in FBRs because of their low irradiation swelling rates. However, their use with carbide fuels was rather limited.

Two steels were examined, the (V, Nb)-stabilized DIN 1.4988 and the titanium-stabilized DIN 1.4970 steels. The weight concentration of V + Nb in the former amounts to ~ 1.5 %, whereas in the latter the titanium concentration does not exceed 0.6 %. In both cases, 15 % cold-worked material was used. The carburization behavior of these stabilized steels displays essential differences with respect to Type 316 stainless steel.

The measured carburization hardening on the inner cladding surface as a function of temperature shows a maximum located between 750 and 830 K for the titanium-stabilized steel and between 850 and 900 K for the (V, Nb)-stabilized ones (Fig. 15), and the hardness values attained are significantly higher than in Type 316 stainless steel. However, the carburization depth is comparatively low for temperatures up to 850 K. At higher temperatures the carburization becomes deeper, but the hardening decreases (Fig. 16).

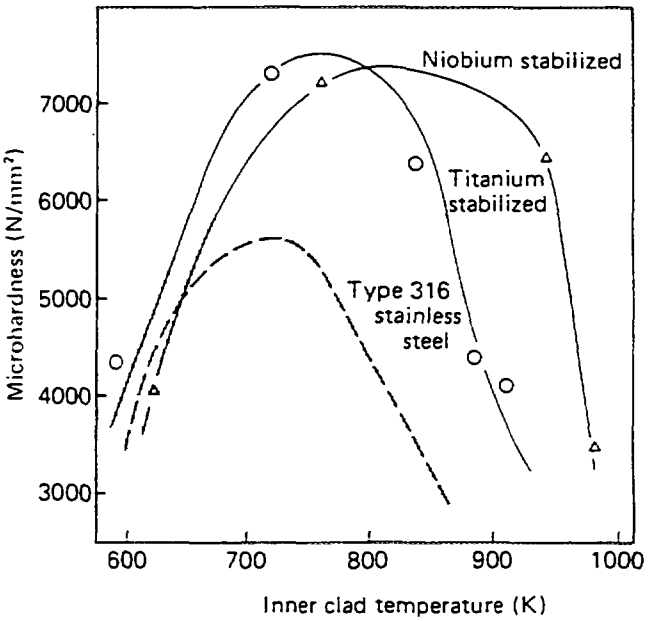

Fig. 15 Maximum observed hardening caused by carburization in sodium bonded pin cladding after a burnup of ~8% fima. The curves represent the behavior of the Ti- and (V,Nb)-stabilized steels, as compared to Type 316 stainless steel (shaded area).

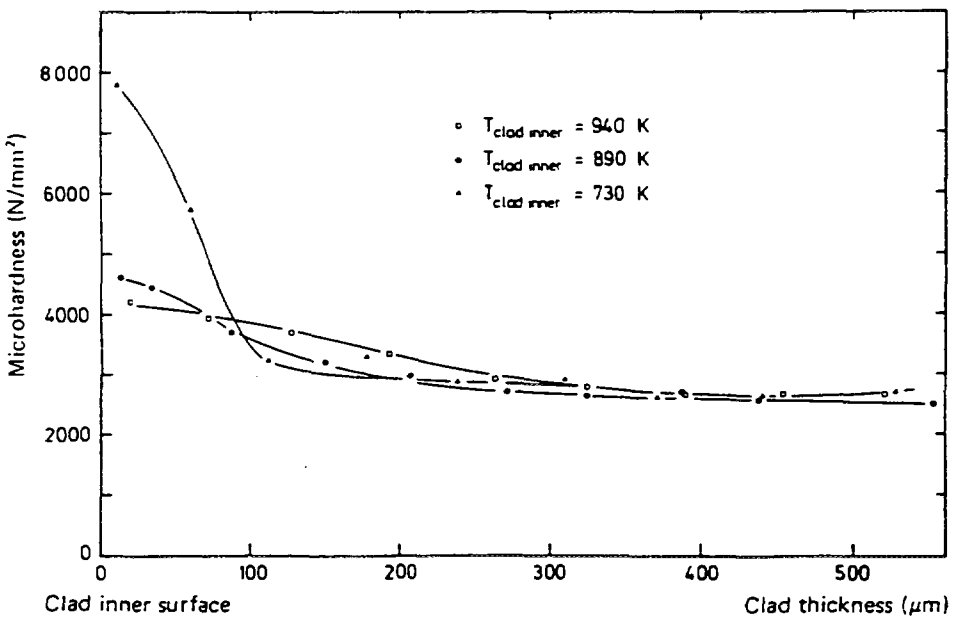

Fig. 16 Microhardness profiles from the inner cladding surface at three temperatures for a titanium-stabilized steel.

In the high-temperature range explored (850 to 1000 K) in the niobium-stabilized steel, grain boundary carbide precipitation is observed beyond the carburization layer over the whole cladding cross section. This effect is less pronounced in the titanium-stabilized steel. Generally, the carburization reactions in stabilized steels are faster than in non-stabilized alloys. In particular, between 850 and 1050 K the precipitation rate of carbide is increased up to one order of magnitude. For instance, in niobium-stabilized steels containing 130 ppm carbon at 850 K, $M_{23}C_6$ is observed to precipitate on the grain boundaries and Nb(C, N) within the grains after only 10 h of annealing.

The reaction patterns leading to the precipitation of titanium or niobium carbides are rather complex (see, for example, Ref. 6), involving formation of metastable compounds followed by re-solution stages. However, since the stabilizing elements have significantly lower diffusion coefficients in steel than chromium, these reactions, in the temperature range of interest (600 to 1000 K) occur with formation of finely dispersed precipitates.

These features explain the high degree of hardness achieved by the stabilized steel after carburization. Even the displacement of the maximum in the hardening curves toward higher temperatures (see Fig. 15) is probably associated with the persisting intragranular precipitation controlled by the less mobile stabilizers. These observations indicate that the loss of ductility caused by carburization in stabilized steels is probably more pronounced than in Type 316 stainless steel. From the measurement of carburization depths and hardness, it is expected that the highest cladding failure risk, produced by carburization, is encountered in the intermediate temperature range between 800 to 900 K, i. e., at a somewhat higher temperature than in Type 316 stainless steel.

3.6 Conclusions

The following conclusions can be drawn:

1. Solution annealed austenitic steels of Type 316 do not seem to be suitable as cladding materials for MC. The carburization produced by standard hyperstoichiometric fuels is very deep. At high burn-up, nearly 50 % of the cladding volume is expected to suffer a dramatic loss of ductility. Several irradiation tests confirm that claddings of solution-annealed Type 316 stainless steel deformed by 0.5 to 1 % exhibit numerous radial cracks extending from the internal cladding surface through the heavily carburized region, with a depth of > 200 μm. Under tensile stresses exerted by the fuel or caused by thermal cycling, these cracks evolve very rapidly into severe cladding breaches.
A significant percentage of pins was observed to fail after diametral deformations of < 1.5 %.

2. Stabilized steels, which are presently considered because of their low irradiation swelling, display worse carburization properties at temperatures> 900 K.

3. Among the cladding materials that are presently customarily used, cold-worked Type 316 stainless steel seems to provide the best resistance to carburization, although this observation is based on incomplete evidence.

4. Finally, ferritic alloys could offer substantial advantages with respect to austenitic steel: Their carbon content is approximately one order of magnitude higher than that of Type 316 stainless steel (0.3 % maximum versus 0.4 % maximum), and their mechanical properties are little influenced by carburization levels. Ferritic steels, which develop maximum softness, ductility, and corrosion resistance in the annealed condition, can be suitably tailored in order to obtain the best compromise between a high room-temperature ductility and an elevated stress rupture strength at high temperature. Recently, a 13 Cr-Ti-Mo ferritic alloy was obtained showing low sensitivity to embrittlement and swelling under fast neutron irradiation and an excellent compatibility with sodium. Adversely, one could fear that placing pins with ferritic steel cladding in an (presently) otherwise austenitic steel-sodium system would induce a carbon transfer through the coolant channels with possible detrimental effects. The experimental results obtained to date are very encouraging, showing a pronounced insensitivity of the carbon concentration in these ferritic alloys to variations of carbon activity in sodium.

References

1. C. Ronchi, M. Coquerelle, H. Blank, J. Rouault, 'The Sodium-Bonding Pin Concept for Advanced Fuels', Part II: Analysis of the Cladding Carburization, Nucl. Techn., **67** (1984) p. 73

2. G. Gotzmann, P. Hofmann, and F. Sarikaya, 'Mechanical Properties of Cladding Materials after Annealing with Carbide Fuels', KfK-1942, Kernforschungszentrum Karlsruhe (1973)

3. A. Thorley and C. Tyzak, 'The Carburization of Stainless Steel in Sodium containing Carbon Impurities and its Effects on Mechanical Properties', Proc. Conf. Effects of Environment on Mechanical Properties in Nuclear Systems', British Nuclear Energy Society, London (1971)

4. H. R. Brager, F. A. Garner and E. R. Gilbert, 'Stress-Affected Microstructural Development and the Creep-Swelling Interrelationship', Proc. Conf. Radiation Effects in Breeder Reactor Structural Materials, Scottsdale, Arizona, p. 727, American Society for Testing and Materials (1977)

5. W. V. Wayda and K. Ehrlich, 'Radiation-Induced Recrystallization, its Cause and Consequences in Heavy-Ion irradiated 20 % Cold-Drawn Steel of Type 1.4970', J. Nucl. Mater., **113**, 149 (1983)

6. H. Gerlach and E. Schmidtmann, 'Einfluß von Kohlenstoff, Stickstoff und Bor auf das Ausscheidungsverhalten eines Austenitischen Stahles mit 16 % Cr 2 % Mo 16 % Ni und Niob', Arch. Eisenhüttenwesen, **39**, 1 (1968)

7. R. P. Agarwala, M. C. Naik, M. S. Anand and A. R. Paul, 'Diffusion of Carbon and Stainless Steels', J. Nucl. Mater., **36**, 41 (1970)

4. A Head-End Gaseous Oxidation Process for Irradiated Carbide, Carbonitride, Nitride Fuels

4.1 Introduction

Extraction of unspent uranium and plutonium from irradiated oxide fuel is performed by the well established PUREX process. Advanced fuels (carbides, carbo-nitrides, nitrides) could be handled by this process after conversion to the oxide. In principle, this may be performed by a wet chemical process (but this involves the production of complex organic molecules which interfere with the extraction process) or as in the study reported here, by gaseous oxidation (Ref. 1, 2).

For easy reprocessing, the oxidized fuel must be exclusively near stoichiometric (U, Pu)O_2 containing 25 % Pu. Accordingly, samples of advanced fuels have been oxidized in gaseous environments to determine the most appropriate means of achieving the required degree of oxidation. This report summarizes the arguments leading to the choice of oxidizing media used in this study and the analysis of the oxides thus formed.

4.2 Choice of oxidizing media

Thermodynamic calculations indicate that CO/CO_2 mixtures could be used to provide suitable oxidizing media at 700° C - 900° C. Assuming the predominant reaction to be of the type:

$$MC + 3\ CO_2 = MO_2 + 4\ CO$$

then (U, Pu)O_2 should be formed if the CO/CO_2 ratio is maintained between $\approx$ 10/1 and 1/100 at $\cong$ 800° C. It has been estimated that CO_2 alone flowing at $\cong$ 6 l/h through the furnace which in this case had a reaction chamber of $\cong$ 3 l, would result in gas compositions within this range at $\cong$ 800° C; the permissible range of CO/CO_2 ratios gives considerable flexibility in the operation of this process.

In addition, rapidly flowing (50 l/h) Ar-20 % O_2 at 590° C has been employed in some tests. Such a gas would avoid possible additional contamination by carbon from CO/CO_2 mixtures which would lead to residue problems in the PUREX process. Preliminary tests with unirradiated (U, Pu)C indicated that at less than 600° C a product soluble in nitric acid would be formed in this environment (1).

4.3 Experimental techniques and results

Starting materials consisted of sections up to 60 mm long of mixed (U-20 % Pu) irradiated carbide, carbonitride and nitride pins with maximum burn-ups from 1 to 7 at. %; the maximum linear power was 1350 W/cm. During oxidation, the gas was passed continuously over the specimen which was contained in a covered stainless steel crucible in the furnace. Oxidations in CO/CO_2 commenced with an interval of 1 h at 700° C primarily to precipitate carbides in the cladding steel (DIN 1-4970), so that it would fail/crack in a brittle manner from the stresses generated by the volume change on conversion of the fuel to oxide, thus exposing the fuel to the gas. Subsequent oxidation was always at higher temperatures, up to 800° C. Samples of oxidized fuel were mounted, polished and examined on an optical microscope; other samples were studied by X-ray diffraction to determine the O/M rate of the oxide and to determine the presence of other phases.

4.4 Results and discussion

Oxidation in CO/CO" AND Ar-20 % O_2

Table 3 gives details of the fuels which have been oxidized, oxidation conditions and the results of X-ray analysis. Oxidation in CO/CO_2 resulted in exclusive formation of (U, Pu)O_2 with an O/M ratio close to the stoichiometric value. From experience gained previously, little difficulty should be encountered in handling these oxides by the PUREX process. Oxidation in Ar-20 % O_2 resulted (with the possible exception of sample AP1) in two phase oxides containing significant amounts of M_3O_8 (see section 2).

Microscopic examination of reaction products

All oxidations in CO_2 resulted, as expected, in brittle intergranular failure/cracking of the cladding. In cases where a longitudinal (fiducial) mark was present on the outside of the cladding, the brittle crack closely followed this mark. Cladding/failure cracking was not observed during oxidation in Ar-20 % O_2.

The morphology of the reaction product did not depend on the type of fuel or on the oxidizing gas (see below) but rather on the fuel restructuring which had occurred during irradiation.

Oxidation in Ar-20 % O_2 only resulted in a surface attack and in some oxidation along major cracks. Scale formed at the fuel/cladding interface and on the exposed (cut) faces at the ends of the pin section and grew progressively into the fuel.

At the end of the oxidation (little or no further change in weight of the samples), the oxidized fuel consisted of a powder of particle size 10 - 50 μm, regardless of the oxidizing medium and type of fuel.

4.5 Conclusions

1) Conversion of advanced fuels (carbide, carbo-nitride and nitride) to oxide by heating in flowing CO_2 at ≅ 800° C offers a promising alternative to the wet chemical process.

2) Oxidation in Ar-20 % O_2 carried out at 590° C does not always result in exclusive formation of near stoichiometric (U, Pu)O_2.

3) Since the particle size of the oxide is 10 - 50 μm, a high percentage of the fission products will be present in the oxide.

4) Oxidation of the advanced fuel proceeds both at the outer surface and also internally (on the inside of pores, along cracks etc.) when flowing CO_2 is used at ≅ 800° C.

References

1. U. Benedict, K. Richter, and G. J. Tuerlinx, Trans. of ENC '79 Conf. of European Nuclear Soc., Hamburg, 1979, 31. TANSA 1-666 (1979) p. 512

2. A. L. Mills and K. Hartley, British Patent 1 205 169 (1968)

The experimental results collected in this report have been obtained by Dr. H. Blank, U. Benedict, C. Ronchi, I. Ray, C. T. Walker, B. Whitlow and M. Coquerelle.